In-situ visualisation of the micro-structure of a Carbopol gel during a confined microscopic flow

Eliane Younes, Michal Himl, Zdenek Stary, Teodor Burghelea

In-situ visualisation of the micro-structure of a Carbopol gel during a confined microscopic flow

Eliane Younes

Université de Nantes, CNRS, Laboratoire de Thermique et Energie de Nantes, UMR 6607, La Chantrerie, Rue Christian Pauc, B.P. 50609, F-44306 Nantes Cedex 3, France

Michal Himl

Department of Organic Chemistry, University of Chemical Technology Prague, Technická 1905/5, 166 28 Prague, Czech Republic

Zdenek Stary

Institute of Macromolecular Chemistry Czech Academy of Sciences, Heyrovskeho nam. 2, 162 06 Prague, Czech Republic

Teodor Burghelea

Université de Nantes, CNRS, Laboratoire de Thermique et Energie de Nantes, UMR 6607, La Chantrerie, Rue Christian Pauc, B.P. 50609, F-44306 Nantes Cedex 3, France

Abstract

An in-situ visualisation of the microstructure of a Carbopol gel flowing in a micro-channel is presented. By means of a novel chemical protocol able to stain the solid material units of the gel with a fluorescent molecule we are able to accurately identify the solid/fluid material units advected by the confined microscopic flow. Based on this novel visualisation technique a full statistical description of the distributions of solid-fluid material units in the flow in terms of space and time averages, probability density functions and space-time correlations is reported for the first time.

Email addresses: Eliane.Younes@univ-nantes.fr (Eliane Younes), michal.himl@vscht.cz (Michal Himl), stary@imc.cas.cz (Zdenek Stary), Teodor.Burghelea@univ-nantes.fr (Teodor Burghelea)

1. Introduction

Yield stress materials represent a broad class of materials that behave as solids unless a critical shear stress coined as the *"yield stress"* $\tau = \tau_y$ is applied onto them.

From a historical perspective, the first models to describe the yielding behaviour were the Bingham model [3] and the Herschel-Bulkley model [17]. Both models predict an abrupt solid fluid transition that occurs at a well defined value of the applied stress, $\tau = \tau_y$, followed by a viscous flow regime which is Newtonian in the case of the Bingham model and shear thinning in the case of the Herschel-Bulkley model. None of these two empirical models is able to predict/describe any other physical feature of the solid-fluid transition.

During the past several decades, a significant progress has been made in understanding the rheology and flows of visco-plastic materials particularly on an experimental side, [23, 23, 1, 5].

The theoretical understanding of yielding and flows of viscoplastic materials has significantly progressed as continuous macroscopic models bearing features absent in the classical Bingham/ Herschel-Bulkley models have been developed, [46, 41, 42, 11, 32, 31, 33].

A step forward in understanding the solid-fluid transition was to describe the response of the material to an external forcing in terms of a micro-structural parameter Φ that varies smoothly between $\Phi = 1$ corresponding to the solid state to $\Phi = 0$ in a fluid state. Such phenomenological models have been proposed by various authors [13, 32, 31, 33, 9, 10, 35, 29, 41, 42, 11, 12, 4] and have a general form:

$$\frac{d\Phi(t)}{dt} = F_1\left[\Phi(t), \tau(t), C_1, C_2, ..., C_m\right] \tag{1}$$

Whereas a number of authors attribute to the structural variable Φ the generic meaning of a measure of the *"degree of structuring"* of the material, e. g. [41, 42, 14] or *"fluidity"* [27] we prefer to think of it in terms of a volume fraction of solid as done, for example, by Prof. Daniel Quemada in a sequence of papers [32, 31, 33]. The motivation for this choice is two-fold. First, from a fundamental perspective, the volume fraction of solid has a sound (rather than an elusive) physical meaning of mass of the solid material elements and therefore satisfies the mass conservation. Second, unlike the *"fluidity"* or the even more generic and physically elusive *"degree of structuring"*, this quantity is accessible to direct (in-situ) microscopic scale measurements that are both space and time resolved. The distinctive feature of these micro-structural models is that they describe the temporal evolution of a micro-structural parameter $\Phi(t)$ as a function of the applied stress τ and a number of parameters $C_1, ..., C_m$. Part of these parameters describe the kinetics of the destruction/re-structuration of the material and are often difficult (or impossible!) to measure. The rest of the parameters describe the rheological behaviour of the material (e.g. yield stress, consistency, power law index, elastic modulus) which may be measured via adequate macroscopic rheological tests (flow ramps, oscillatory measurements,

creep/relaxation tests etc.). The functional dependence described by Eq. 1 is often chosen on a phenomenological (and semi-empirical) basis rather than based on first principles describing the microscopic scale dynamics in terms of molecular scale interactions. The micro-structural equation 1 needs to be complemented by a constitutive relationship which takes the general functional form:

$$\tau(t) = F_2\left[\Phi(t), \frac{d\tau\,(t)}{dt}, \dot{\gamma}(t), A_1, A_2, ..., A_m\right] \tag{2}$$

where $\dot{\gamma}$ is the rate of deformation and the material constants $A_1, A_2, ..., A_m$ reflect the rheological behaviour of the material.

Poly-acrylic polymers synthesised in the $1950's$ (Brown, H.P., Carboxylic polymers, US Patent 2798053A, 1957) and commercialised under the generic trade name of *Carbopol* are generally considered as nearly *"ideal"* yield stress materials in the sense they exhibit minimal thixotropy, are chemically stable for indefinite periods of time and, sufficiently far from the yield point, their rheometric behaviour can be described well by the simple Herschel-Bulkley constitutive relationship. Near the yield point, however, the Herschel-Bulkley relationship performs poorly, [50, 7, 29, 30]: the yielding process of Carbopol gels is gradual, the rheological response depends on the rate at which the material is loaded/unloaded and, when unloaded, non-negligible elastic effects are observed. For the particular case of Carbopol gels, a basic requirement for the functional dependencies F_1 and F_2 is that in the asymptotic limit $\Phi \to 1$ one recovers an elastic solid behaviour described by Hooke's law and in the asymptotic limit $\Phi \to 0$ one recovers a shear thinning behaviour described by the Herschel-Bulkley law, $\tau = \tau_y + K\dot{\gamma}^n$. Here K is the consistency of the gel, $n \in (0, 1)$ the power law index and $\dot{\gamma}$ is the shear rate. Although able to fit different types of rheological measurements, such models provide a limited amount of information about the dynamics of the solid-fluid transition. This inherent drawback comes from the fact that evolution equations such as Eq. 1 are often derived on an intuitive basis rather than from first principles applied to the microscopic material constituents. This issue has been clearly highlighted in a recent review article, [5]: *"It should therefore come as no surprise that no complete, well-accepted, first-principle theoretical approach exists that can account for all aspects of the rheology of yield stress materials"*. It is therefore safe to state that from the point of view of first principles governing the microscopic scale physics the solid-fluid transition remains *'elusive"* which motivates in part the present contribution.

A microscopic model derived from basic principles of the Statistical Physics and able to capture the yielding behaviour of yield stress materials in general and of Carbopol gels in particular was proposed only very recently in Refs. [36, 37]. Its continuous variant (i.e. the derivation of a differential evolution equation for the micro-structural parameter Φ) was reported in a subsequent paper, [8]. The key novel idea proposed in Refs. [36, 37, 8] is that the microscopic physics of yielding of a viscoplastic material could be described using statistical tools rather than a deterministic approach as the classical viscoplastic models do. To our best knowledge, these ideas have never been tested experimentally which is

most probably due to the difficulty of measuring the in-situ dynamics of solid and fluid material elements. The global aim of the present contribution is to provide a systematic in-situ description of the micro-structure of a Carbopol gel flowing in a confined microscopic environment. The existing information on the micro-structure of Carbopol gels is rather scarce. It is generally believed that Carbopol dispersions consist of highly swollen deformable particles that become space- filling above a critical concentration Φ^*. The evidence for this is, however, indirect. The first observations of a spongy micro-structure of Carbopol gels we are aware of were made by means of Scanning Electron Microscopy (SEM) performed on quiescent and frozen gel samples, [26]. As freezing the sample leads to the appearance of ice crystals which disrupt the soft gel micro-structure, such observations should be interpreted with great caution.

Oppong and coworkers have studied the microscopic diffusion of nano tracers within a quiescent Carbopol sample and concluded that the micro-structure of the gel is strongly heterogeneous, Refs. [25, 24]. The nano tracer particles were found to be confined inside spongy-like structural elements of the gel. For low polymer concentrations, the tracers are likely to escape their initial structural element, but they get trapped in a neighbouring one. For higher Carbopol concentrations the degree of confinement of the nano tracers was higher and their escape probability is lower. The same group have attempted to visualise the Carbopol micro-structure by staining the gel with a cationic dye, Acridine Orange, [16]. Whereas in an acid state (when the material has practically no yield stress) they could clearly see a microstructure (see Fig. 8 therein), in a neutral state (the sample had measurable yield stress) a micro-structure could no longer be observed. This result can be easily understood bearing in mind that an ionic staining of the Carbopol sample relies on the existence of free charges on the backbone of the polymer which vanish upon the neutralisation.

Here we report for the first time direct observations of the micro-structure of a Carbopol gel during a confined micro-channel flow based on a novel covalent staining procedure of the Carbopol backbone with a fluorescent die combined with in-situ observation of the flow by means of two-colour epi-fluorescent microscopy.

The paper is organised as follows. The experimental methods are described in Sec. 2. A particular attention has been devoted to the description of the microfluidic flow system Sec. 2.1, preparation of the Carbopol gel Sec. 2.2, the covalent staining of the gel micro-structure with Rhodamine Sec. Appendix A, the digital image processing techniques to identify the Carbopol micro-structural units from the fluorescent images Sec. 2.4 and the measurements of the flow fields Sec. 2.5.

The results are presented in Sec. 3. The structure of the confined microscopic flow is detailed in Sec 3.1. The statistics of the distributions of the solid/fluid material units in the flow assessed via space and time resolved measurements of the volume fraction of solid material units is described in Sec. 3.2. A systematic analysis of the space and time correlations characterising the distributions of solid material units in the flow is presented in Sec. 3.3.

The paper closes with a summary of the main experimental findings and a

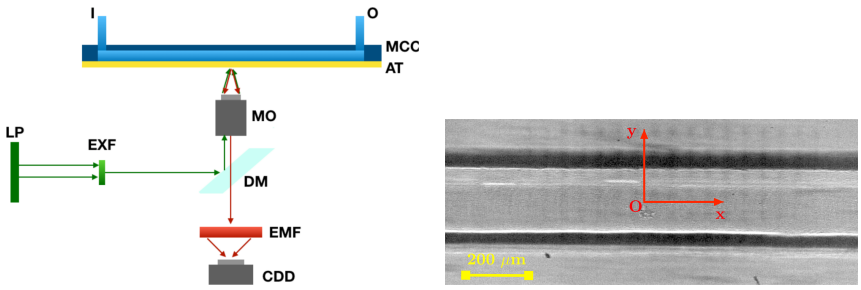

(a) (b)

Figure 1: (a) Schematic view of the microfluidic experimental setup: **MCC**: micro-channel chip, **I**: micro-channel inlet, **O**- micro-channel outlet, **AT**- adhesive tape, **MO**- microscope objective, **DM**- dichroic mirror, **LP**- light emitting lamp, **EXF**- excitation filter, **EMF**- emission filter, **CCD**- digital camera. (b) Micro-graph of the micro-channel. The image was acquired in white light.

discussion of their possible impact on our current understanding of the microscopic yielding of a physical gel, Sec. 4.

2. Experimental methods

2.1. Experimental setup

The experiments have been performed in a straight micro-channel with a rectangular cross section. The width of the micro-channel is $W = 200\ \mu m$, its depth is $H = 50\ \mu m$ and its length $L = 4\ cm$.

The micro-channel was machined from an acrylic block with the dimensions $5\ cm \times 3\ cm \times 0.5\ cm$ using a fast spinning ($14000\ rot/min$) micro-milling head (Nakanishi, model $HES510 - BT40$) mounted on a commercial computer controlled milling machine (Twinhorn, model $VH1010$). For a detailed description of the technique we refer the reader to Ref. [21]. By a precise alignment of the initial acrylic block on the stage of the milling machine, the depths of the micro-channel was uniform over its entire lengths with an end to end variation smaller than one percent. The average roughness of the edges of the micro-channel as resulted from the micro milling process is roughly of the order of a micron which accounts for half percent of the channel width, Fig. 1(b). The edge smoothness obtained with this micro-machining technique is comparable to that obtained via the classical micro lithography techniques used to produce $PDMS$ micro-channels, [45]. The micro-channel was sealed with a strong and optically transparent adhesive tape ($3M$, model $727-1280$). The micro-channel chip is mounted on an inverted epifluorescent microscope (Axio Observer A1, serial no3832002215), Fig. 1(a).

The microscopic flows have been visualised through a $20X$ magnification objective (Zeiss EC Plan-NEOFLUAR 20x/0,5) with a numerical aperture $NA = 0.35$ and a long working distance $WD = 70\ mm$. The microscope is equipped with a set of filters that allow one to visualise in either green or blue fluorescent

light. The microscopic flows were generated using a high precision micro-syringe pump (KdScientific, model Legato 110). To insure a steady flow rate Q which was crucial for this study, we have used a 10 ml gas tight syringe (Hamilton, model $1010LT$). The flows were illuminated with a powerful halogen lamp coupled to the inverted microscope.

A series of flow images was acquired corresponding to each value of the flow rate Q with a digital camera, Prosilica GE camera with 16 bit quantisation (model GE680C from Allied Technologies). The images were acquired at the mid-plane of the micro-channel and at mid-distance downstream.

2.2. Preparation of the Carbopol gel, rheological characterization

The working fluid was an aqueous solution of Carbopol Ultrez 10 with the concentration of 0.1 $wt\%$. Carbopol is the generic trade name of a cross-linked polyacrylic acid $-[CH_2 - CH(COOH)]-$ with high molecular weight. In an anhydrous state, it is commercialised in the form of a white powder soluble in aqueous solvents. After the addition of a neutralising agent such as sodium hydroxide ($NaOH$), a clear gel is obtained.

The Carbopol gel was prepared according to the following protocol. First, the Carbopol was labelled with Rhodamine B at the Department of Organic Chemistry, University of Chemical Technology Prague according to the protocol described in detail in Appendix A. Next, the right amount of anhydrous and fluorescently labelled Carbopol was dissolved in deionised water using a magnetic stirring device at a speed of 1000 rpm. The degree of mixing/dissolution was assessed visually by monitoring the optical isotropy of the solution. In addition to the Rhodamine staining described in Sec. Appendix A which was performed prior to the dissolution in water, 100 parts per million of fluorescent micro-spheres with a mean diameter of $2\mu m$ (Fluoro Max, $B0200$ from ThermoFischer Scientific) have been added to the solution of Carbopol solution. Unlike the Rhodamine which fluoresces when illuminated with blue light the micro-spheres fluoresce only when illuminated with green light. Next, the pH of the solution was gradually increased from 3.2 to 7 by titration with small amounts of a 10 $wt\%$ aqueous $NaOH$ solution gradually pipetted while gently mixing the solution. The rheological characterisation of the solution was performed after seeding the Carbopol solution with the fluorescent tracers and after the covalent staining procedure. Measurements of the dependence of the absolute value of the rate of deformation on the imposed stress were performed using a controlled stress ramp for both increasing and decreasing values of the applied stress, Fig. 2. As previously detailed in a number of papers where various grades of Carbopol were characterised in the absence of a fluorescent labelling, [29, 47, 28, 43, 50], a hysteresis is systematically observed upon increasing/decreasing stresses around the solid-fluid transition.

The yield stress of the final working solution was found via a classical Herschel-Bulkley fitting procedure (the full line in Fig. 2), $\tau_y \approx 1.8 \pm 0.2 Pa$, the consistency $K = 0.8 \pm 0.05\ Pas^n$ and the power law index $n = 0.6 \pm 0.1$. These values together with the shape of the increasing/decreasing stress ramps exhibiting a hysteresis around the yield point reproduce very well the measurements

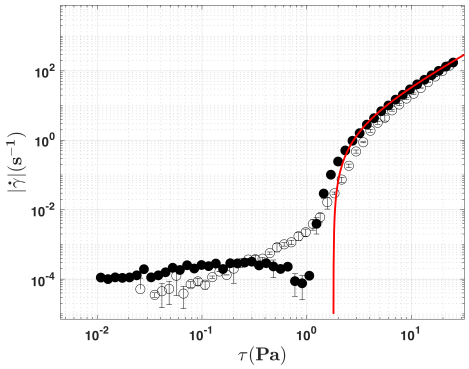

Figure 2: Rheological measurements of the dependence of the absolute value of the rate of strain $\dot{\gamma}$ on the applied stress. The data were averaged during $7s$ corresponding to each value of the imposed stress. The error bars are defined by the root mean square deviation of the results obtained from four distinct runs performed with fresh samples. The full line is a nonlinear fitting function according to the Herschel-Bulkley model.

performed with un-labelled Carbopol. By this we conclude that the covalent staining of the Carbopol with Rhodamine B did not alter in any measurable way the rheological properties of the solution used in our experiments.

Through the rest of the paper we chose to identify the flow states by the plasticity number, [44]:

$$Pl = \frac{\tau_y}{\tau_y + K\left(\frac{2U_{av}}{W}\right)^n} \tag{3}$$

where U_{av} is the mean flow speed computed using the flow rate and the cross-sectional area of the micro-channel $U_{av} = \frac{Q}{WH}$. By varying the flow rate Q the plasticity number was varied in the interval $Pl \in [0.0096; 0.25]$. We note, however, that while computing the plasticity number we did not account for the wall slip effects (that are systematically diminishing the characteristic shear rate $\frac{2U_{av}}{W}$) so the values we display should solely be interpreted as *"nominal values"* and regarded with a fair amount of caution.

2.3. Image acquisition

For each value of the flow rate, two consecutive image acquisition steps were performed: a first one in blue light ($\lambda = 488\ nm$) in order to visualise the Carbopol micro-structural units labelled covalently with Rhodamine while the micro-spheres were invisible and a second one in green light ($\lambda = 532\ nm$) in order to visualise the seeding particles while the Carbopol micro-structure was invisible.

The first batch consisted of 3000 subsequent images which was processed following the steps described in Sec. 2.4. The second batch consisted of another 3000 subsequent images and was processed following the steps described in Sec. 2.5.

2.4. Image processing for the quantitative assessment of the distributions of solid and fluid material elements in the flow

The processing steps of the first batch of images are illustrated in Fig. 3. The first step was to compute the average background over all raw images similar to the one exemplified in panel **(a)** of Fig. 3. Second, in order to correct for systematic non-uniform illumination, each raw image has been divided by the background, panel **(b)**. As a third step the contrast of each image was enhanced using an adaptive histogram technique provided by the *Image Analysis* toolbox of Matlab, panel **(c)**. Next, the contrast enhanced image has been binarised, panel **(d)**. Last, the contour and centroid of each micro-structural element of the Carbopol gel have been determined, panel **(e)** of Fig. 3. This final binary image reflects the distributions of solid material units. The contours of each solid material element represent the solid-fluid interface.

2.5. In-situ measurements of the flow fields

The main tool used to systematically characterise the microscopic flow using the second batch of images was an adaptive multi-grid Digital Particle Image Velocimetry (DPIV) (see Refs. [39, 34] for a detailed description of the method) entirely developed in house under Matlab (together with the *"Image Processing Toolbox"*) which followed the steps briefly described below. First, a background was calculated by averaging all the images of the first time series we have acquired. Second, the average background was subtracted from each image of the sequence. These steps insure an automatic correction for non-uniform brightness of the field of view which may trigger spurious velocity measurements. Finally, pairs of pre-processed images separated in time by the inter-frame t_1 are passed to a multi-pass $DPIV$ algorithm using a sequence of squared interrogation windows with sizes $[128, 64, 32, 16, 8]$ pixels. Small velocities are resolved by a sub-pixel interpolation algorithm.

As a post-processing step, each computed velocity field obtained from the $DPIV$ algorithm was filtered using a median filter. The spatial resolution of the velocity fields was 4.5 μm (44 times smaller than the width of the channel). We have shown in a previous study [49] that, within this range of flow speeds our technique is able to measure flow fields with an instrumental error that never exceeded 5% of the measured value.

3. Results

3.1. Structure of the confined microscopic flow

Prior to describing the dynamics of the solid and fluid structural units in the flow we describe the structure of the microscopic flow. An instantaneous flow field measured via the $DPIV$ technique described in Sec. 2.5 is illustrated in Fig. 4. Quite surprisingly for the low Reynolds (Re) number flow of an elasto-viscoplastic material, a clear secondary fluid motion along the y direction (see Fig. 1(b)) is observed. To gain further insights into the microscopic dynamics of the flow, we build a space-time diagram of the modulus of the velocity by

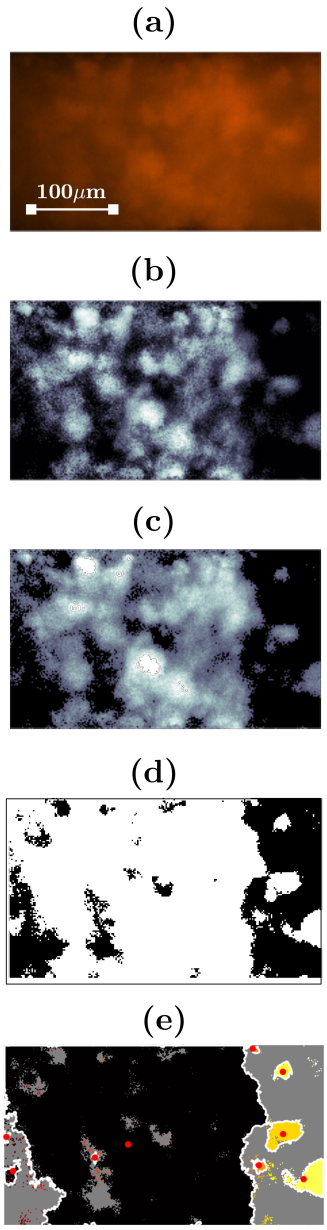

Figure 3: Illustration of the image processing steps for the in-situ identification of solid material units in the flow: **(a)** Original RGB image **(b)** Image converted to grayscale and corrected for the non-uniform brightness of the field of view (see text for description)**(c)** Image after enhancement of the contrast. An animated version can be visualised here. **(d)** Binarised image **(e)** Contours of the detected objects (solid structural units of the gel) representing the solid-fluid interfaces. Their centroids are represented as red solid circles.

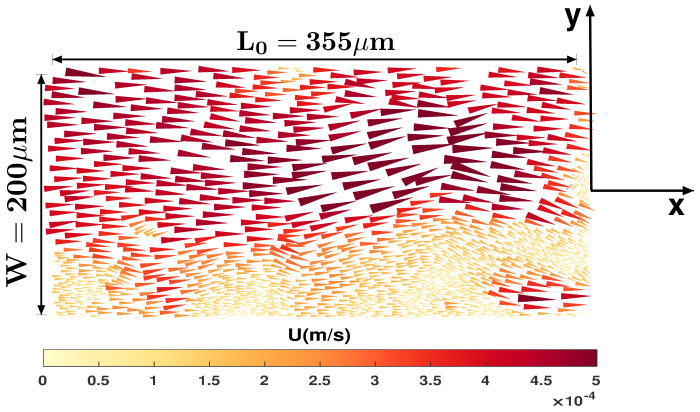

Figure 4: Example of instantaneous flow field measured by means of micro-PIV. The flow rate was $Q = 0.25\mu L/min$. An animated version of the figure may be seen here.

recording the transversal profile of axial velocity at a fixed axial position corresponding to the centre of the field of view, Fig. 5(a). The space-time diagram clearly reveals a time dependent flow. Once more, as $Re < 1$, this effect can not be attributed to fluid inertia. As our channels have a depth H four time smaller than the width, we believe that this effect emerges from the high degree of confinement of the flow. As clearly visible in Fig. 3, solid material units with characteristic sizes of the order of the depth of the channel $H = 50\mu m$ are present in the flow. Their temporal evolution is illustrated in the movie we include as a supplemental material. Such large solid material elements jam the channel for extended periods of time (of order of seconds) while smaller solid material units may still flow past them. We did not observe this phenomenon in our recent investigation of the microscopic flows of a Carbopol gel reported in Ref. [49] most probably because the micro-channel used in these experiments had a significantly larger depth, $H = 200\mu m$. The emergence of secondary flow and time dependence of the flow fields relates to the passage of nearly static regions along the walls of the micro-channel during characteristic times of order of several seconds. A more systematic description of these effects goes beyond the scope of the present contribution and it will be reported elsewhere.

A comparison of the flow fields measurements reported herein with recent results by Liu and De Bruyn [20], however, is somewhat more difficult to make. First, they use a different Carbopol and, as they provide no in-situ measurements of the characteristic size of the solid material units and their space-time dynamics, we have no means of judging whether a similar jamming-like effect occurred during their measurements. Second, the space resolution of their velocity profile measurements is smaller than ours. Third, their measurements were not fully time resolved (no time series of the velocity were shown) so we can not judge if there was any time dependence of their flow fields.

The time averaged transversal profile of the velocity magnitude together with the root mean square deviation (rmsd) of its fluctuations are shown in Fig.

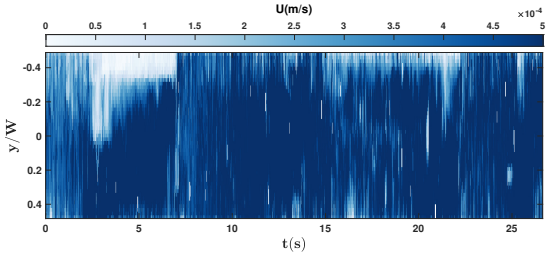

(a)

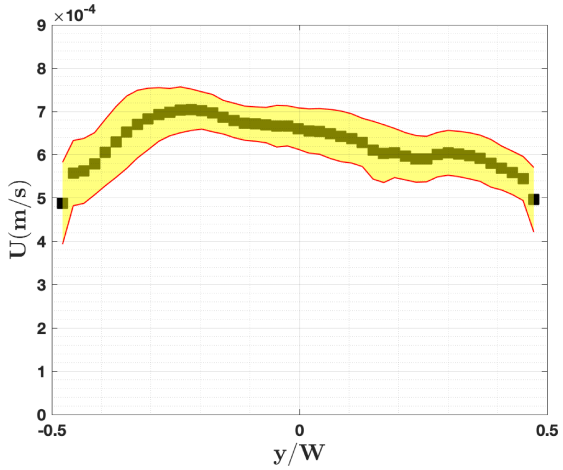

(b)

Figure 5: (a) Space-time diagram of the magnitude of the velocity acquired at the centre of the field of view (see text for description) and a flow rate $Q = 0.25\mu L/min$. The colour maps the magnitude of the velocity. (b) Time averaged transversal profile of the velocity magnitude U. The shaded region highlights the root mean square deviation of the fluctuations of the velocity around its time averaged value (not to be confused with the instrumental error of the velocity measurements which never exceeded 3% of the mean value).

5(b). Flows of viscoplastic materials in channels typically exhibit a central plug region where the axial flow speed is constant. This has been previously observed in both macroscopic channels [28] and microscopic channels with a rectilinear cross-section larger than the characteristic size of solid Carbopol units [49] where no secondary flow and time dependence was observed. Due to the emergence of a secondary flow highlighted in Figs. 4, 5(a) the symmetry of the velocity profile with respect to the centreline of the micro-channel is broken. Also, the level of fluctuations of the flow speed account for roughly 16% of the time averaged value which is significantly larger than the level of the instrumental noise of the $DPIV$ technique which did not exceed 5%. These additional flow features induced by the presence of a strong confinement make the identification of a plug zone in Fig. 5(b) more problematic. Yet, by monitoring subsequent frames of the micro-structural movie (see Movie 3 in the Supplemental material), one notes that statistically speaking, the central zone of the channel is mostly filled with large solid blobs. This indicates that we are actually observing a rigid plug like behaviour though the velocity of the plug varies in time.

3.2. Statistics of the solid-fluid distributions in the flow

A key element in understanding the solid-fluid transition of the gel during the confined microscopic flow refers to the probability distribution of solid/fluid material units in the flow and its relation to the flow rate. To quantitatively assess this, we focus on the statistics of solid material elements passing through the field of view using images of the micro-structure post-processed according to the procedure described in Sec. 2.4 and exemplified in panels (d-e) of Fig. 3. As the bright details of each such image are uniquely related to the presence of solid material units in the flow, the statistics of grey levels of each post-processed image give the average fraction of solid $\langle \Phi \left(\overrightarrow{r}, t \right) \rangle_{\overrightarrow{r},t}$ passing through the field of view. A typical probability distribution function of the volume fraction of solid material passing through the field of view during 15 s is shown shown in Fig. 6.

The measured probability density function are very well fitted by the Weibull probability density function (the full line in Fig. 6):

$$f\left(\Phi;\lambda,k\right) = \frac{k}{\lambda}\left(\frac{\Phi}{\lambda}\right)^{k-1} e^{-\left(\frac{\Phi}{\lambda}\right)^{k}} \tag{4}$$

where $k > 0$ is referred to as the shape parameter and $\lambda > 0$ as the scale parameter of the distribution. The Weibull distribution was initially proposed to describe the strength of the solid materials and the statistics of failure events, [48]. Upon changing the flow rate the probability density functions remain well described by the Weibull distribution. The Weibull distribution typically describes a random fragmentation process where the probability of splitting a solid particle into fragments depends on the size of the particle. Recently, Brown and Wohletz demonstrated that the Weibull distribution arises naturally as a consequence of the fractal nature of the fragmentation process, [6]. According

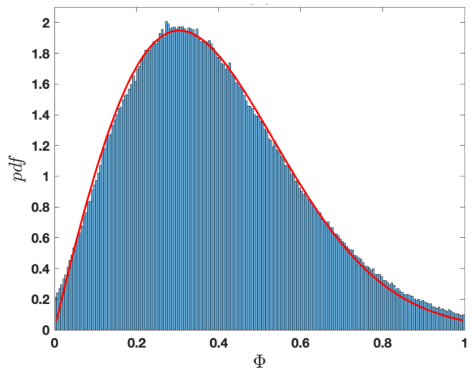

Figure 6: Probability distribution function of the volume fraction of the solid material units passing through the field of view measured for $Q = 0.5\mu l/min$ ($Pl = 0.06$). The full line is a best fit by the Weibull distribution (see text for description).

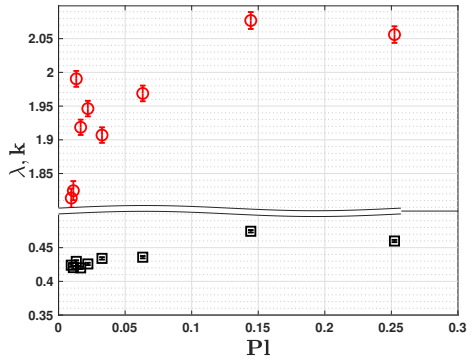

Figure 7: Dependence of the parameters of the Weibull distribution on the plasticity number Pl: squares -λ the scale parameter, circles - shape parameter k. The error bars are defined via the confidence intervals of the nonlinear fit according to the Weibull distribution, Eq. 4

to this scenario, the fragmentation of a solid particle is initiated by generation of a fractal crack tree.

According to the theory of Brown and Wohletz the shape parameter k is related to the fractal dimension d_f characterising the fragmentation process via:

$$k - 1 = \frac{d_f}{3} \tag{5}$$

The dependencies of the parameters of the Weibull distribution obtained by fitting the probability distribution functions displayed in Fig. 6 by Eq. 4 on the driving flow rate Q are shown in Fig. 7. While the scale parameter λ appears to be insensitive to the flow rate, a slight decrease of the shape parameter with the flow rate is observed.

If indeed the size distribution of the solid Carbopol elements resulted from a fragmentation process, we are not sure at what stage this process of the

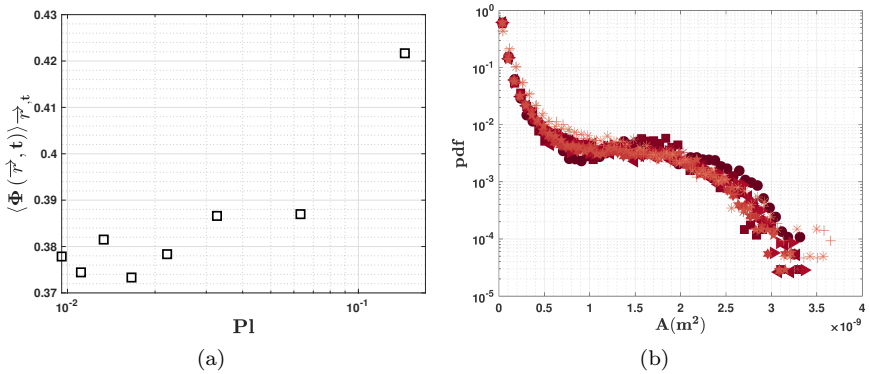

Figure 8: (a) Dependence of the space-time averaged volume fraction of solid material units $\langle\Phi(\overrightarrow{r},t)\rangle_{\overrightarrow{r},t}$ on the plasticity number Pl. (b) Probability distribution functions of the areas of the solid material units measured for all the values of plasticity numbers Pl explored through the manuscript. The statistical ensemble was build during 15 s.

preparation of the solutions this fragmentation process occurred: during the chemical synthesis of the Rhodamine labelled anhydrous Carbopol or during the preparation of the solution (dissolution in water). We are sure, however, that the fragmentation did not occur during the microscopic flow because the probability distributions of the solid blobs were found to be independent on the flow rate.

The first order moment of these distributions is the volume fraction of solid material units averaged in time and over the extent of the field of view $\langle\Phi(\overrightarrow{r},t)\rangle_{\overrightarrow{r},t}$. Its dependence on the plasticity number Pl is shown in Fig. 8(a). The space-time averaged volume fraction decreases monotonically with decreasing Pl and reaches a plateau value $\langle\Phi(\overrightarrow{r},t)\rangle_{\overrightarrow{r},t} \approx 0.375$ corresponding to $Pl \approx 0.03$. It is quite interesting to note at this point that, contrarily to the simple intuition that at low flow rates the space time averaged volume fraction should be close to one (this is the general assumption of the existing phenomenological micro-structural models described by Eqs. 1, 2), the largest value (corresponding to the smallest flow rate investigated) we observe in Fig. 8(a) is significantly smaller, $\langle\Phi(\overrightarrow{r},t)\rangle_{\overrightarrow{r},t} \approx 0.421$. This means that, even in a fully un-yielded state (full plug flow), the solid units are not occupying the entire field of view and alternate with pockets of solvent. This can also be interpreted in terms of a strong spatial heterogeneity of the micro-structure of the gel already pointed out (in the absence of a flow) by Oppong and coworkers [25, 24], and by Gutowski and coworkers [16]. Thus, the simplistic picture of an unyielded Carbopol gel is that of a collection of solid material units in contact with each other (or in a jammed state) which are separated by pockets of solvent. This picture is fully supported by the movie we provide as a supplemental material.

The probability distribution functions of the areas of solid material units

measured for all the flow rates during 15 s are shown in Fig. 8(b).

Quite interestingly, these probability distribution functions are practically independent on the flow rate (or the plasticity number) and all data shown in Fig. 8(b) collapse onto a single sigmoidal shaped master curve. This indicates that the characteristic rates of shear set by the imposed flow rates are too small to sensibly diminish the characteristic size of the solid material units.

3.3. Temporal and spatial correlations of the distributions of the solid material units

The individual images of the micro-structure such as the one exemplified in panel (c) of Fig. 3 indicate a random spatial arrangement of the solid structural units within the micro-channel rather than a well defined solid plug located around the centre line of the channel as typically observed during macroscopic flows of a yield stress fluid, [28]. The animated version of the panel (c) of Fig. 3 available as a supplemental material indicates a random in time passage of solid micro-structural units through the field of view.

These two key observations seem to corroborate well with the theoretical suggestion advanced in Refs. [36, 37, 38] according to which the microscopic dynamics of the solid and fluid elements may be described using statistical tools rather than continuous and deterministic laws. As we now have a novel visualisation tool that allows one to monitor the in-situ dynamics of the solid micro-structural units over extended periods of time (significantly larger than the characteristic time of advection t_a) we can now pursue these ideas for the first time by performing a systematic statistical description of the dynamics of solid-fluid interfaces.

To provide a full and quantitative description of this we focus in the following on the temporal correlations of the solid material units passing through the centre of the field of view. The first step in achieving this is to construct space-time diagrams of the volume fraction of solid by monitoring a transversal (to the mean flow direction) profile of brightness of each image after the compensation step described in Sec.2.4 and exemplified in panel (d) of Fig. 3. Space-time diagrams of the distributions of solid material units built for all the flow rates explored through this study are shown in Fig. 9. The initial intuition on the temporally random advection of the solid material units seems to be confirmed by the appearance of the space-time diagrams which once more justifies a statistical description of the dynamics of the solid-fluid interfaces.

Using the space-time diagrams presented in Fig. 9 one can investigate the temporal correlations of the passage of solid material units through the field of view.

In Fig. 10(a) we present temporal correlations of the distribution of solid material elements measured for a flow rate $Q = 1\ \mu L/min$ ($Pl = 0.03$) in the bulk of the flow within a region of width $\delta_y = 0.1W$ (the curve labelled by a circle) centred around the centre-line of the micro-channel and at a distance $\delta_y = 0.1W$ from the boundary (the curve labelled by a square).

The random passage of solid material units through the field of view is correlated during longer times in the boundary of the flow than in the bulk. This

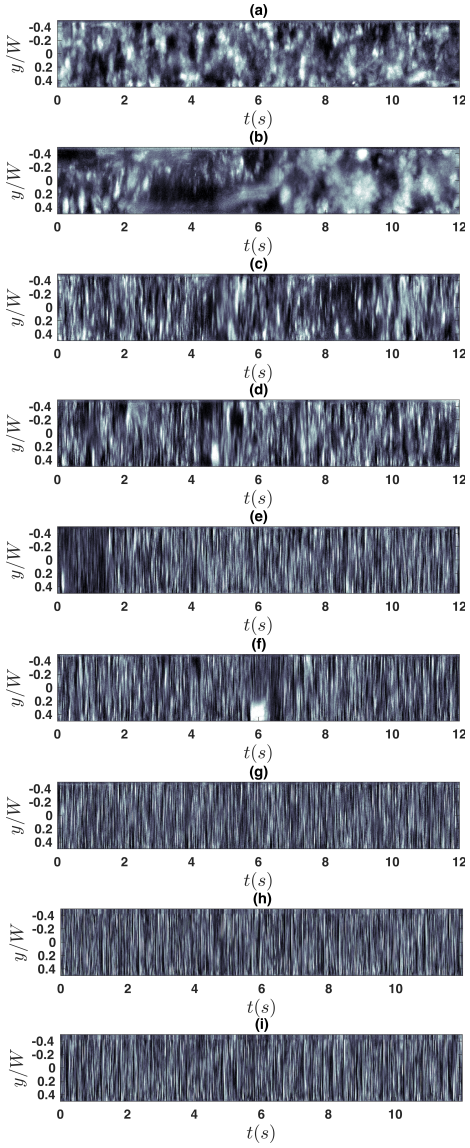

Figure 9: Space time diagrams of the distributions of the solid material units acquired at different flow rates (plasticity numbers): **(a)** - $Q = 0.1\mu L/min$ ($Pl = 0.25$),**(b)** - $Q = 0.25\mu L/min$ ($Pl = 0.14$),**(c)** - $Q = 0.5\mu L/min$ ($Pl = 0.06$),**(d)** - $Q = 1\mu L/min$ ($Pl = 0.03$),**(e)** - $Q = 1.5\mu L/min$ ($Pl = 0.022$),**(f)** - $Q = 2\mu L/min$ ($Pl = 0.016$), **(g)** - $Q = 2.5\mu L/min$ ($Pl = 0.013$),**(h)** - $Q = 3\mu L/min$ ($Pl = 0.011$),**(i)** - $Q = 3.5\mu L/min$ ($Pl = 0.009$).

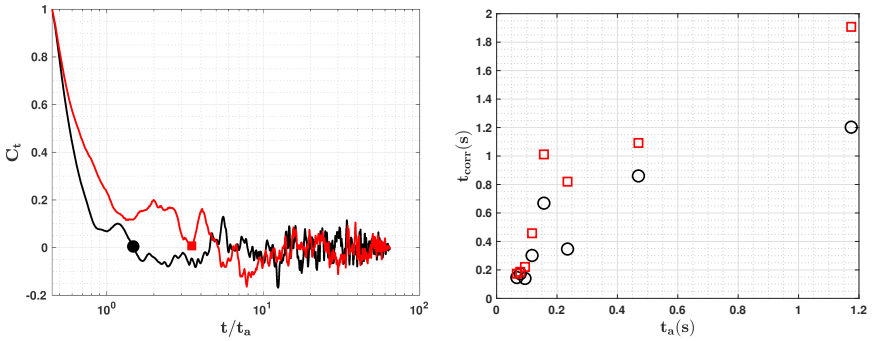

(a) (b)

Figure 10: (a) Temporal correlation functions measured for $Q = 1\mu L/min$ ($Pl = 0.03$) in the bulk (the circle) and the boundary (the square) of the flow (see text for discussion). (b) Dependence of the correlation time measured in the bulk (the circles) and in the boundary (the squares) on the characteristic time of advection t_a.

can be explained on a rather simplistic and intuitive basis as follows. The material units close to the channel boundary experience velocity gradients sufficiently large to inhibit a motion of the solid structural units along a direction transverse to that of the mean flow. On the other hand, the material units close to the centre line of the micro-channel experience a practically null velocity gradient which allows for secondary motion in the form of a translation along the vertical direction or rotation around their centre of mass. The characteristic times of correlation in both the bulk and near the boundary of the flow are defined by the first zero crossing of the correlation functions, Fig. 10(a). A relevant time scale associated to the advection of solid material elements downstream is the characteristic time of advection defined as $t_a = L_0/U_{av}$ where $L_0 = 355\mu m$ is the horizontal dimension of the field of view (see Fig. 4) and $U_{av} = \frac{Q}{HW}$ is the mean flow speed.

The correlation times are comparable in magnitude to the characteristic advection times t_a and, as already exemplified in Fig. 10(a), the dynamics of the solid material elements is, regardless the flow rate (or the plasticity number), longer correlated near the boundary of the flow than in the bulk, Fig. 10(b).

A next important step of the statistical characterisation of the distributions of the solid material units in the flow relates to their spatial correlations. The spatial correlations have been assessed according to a several steps procedure described as follows:

1. For each individual image I^k of the flow post-processed following the steps described in Sec. 2.4 which, by the way it was normalised reflects the instantaneous distribution of the solid material elements in the field of view, we have computed the two dimensional auto-correlation function

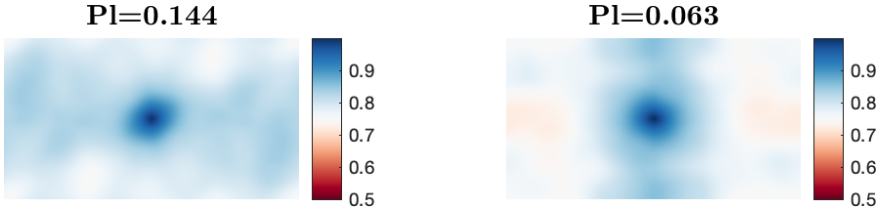

Figure 11: Examples of space correlation surfaces of the micro-structure computed for two plasticity numbers indicated in the top inserts.

defined as:

$$C^k(x,y) = \frac{\left\langle I^k(x+\Delta x, y+\Delta y)\, I^k(x,y)\right\rangle_{\Delta x,\Delta y}}{\left(I^k_{rms}\right)^2} \tag{6}$$

Here I^k_{rms} stands for the root mean square fluctuations of brightness of the image I^k. The time averaged two dimensional correlation function has been computed as $C(x,y) = \left\langle C^k(x,y)\right\rangle_k$.

2. The longitudinal and transversal to the flow direction components $C_x(y) = C(0,y)$ and $C_y(x) = C(x,0)$ have been extracted from the time averaged two dimensional correlation function $C(x,y)$. From each one dimensional correlation the plateau value observed for large values of the arguments has been subtracted and the result was finally normalised by its maximal value.

Spatial correlation maps of the solid structural units of the material are illustrated in Fig. 11 for two flow rates. Unlike Geraud and coworkers who measured isotropic spatial correlation functions, [15], the correlation surface becomes anisotropic when the flow rate is increased (the plasticity number decreased). This can be explained by the fact that our measurements are performed in-situ, i.e. in the presence of a flow while the measurements illustrated in Fig. 5 of Ref. [15] were performed in quiescent conditions.

Measurements of the one dimensional correlation functions performed both along and across the flow direction are exemplified in Fig. 12(a). Both spatial correlation functions are found to be independent of the plasticity number (Fig. 1 in the Supplemental material). The spatial anisotropy of the spatial correlations already noted in Fig. 11 becomes even more clear: the distributions of solid material units are stronger correlated along the flow direction than in a direction transversal to flow.

Both spatial correlation functions decay exponentially:

$$C_r = C^0_r exp\left(-\frac{r}{\Delta r}\right) \tag{7}$$

with $r = x, y$ and the correlation distances $\Delta r = \Delta x_c, \Delta y_c$. These exponentially decaying correlations allow one to measure the characteristic correlation distances $\Delta x_c, \Delta y_c$, Fig. 12(b).

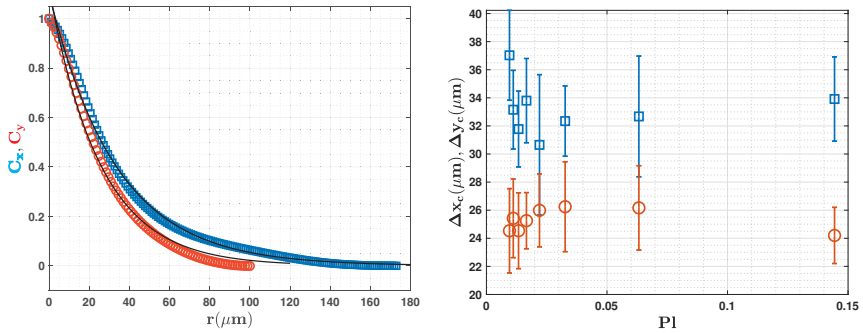

(a) (b)

Figure 12: (a) Spatial correlation functions of the distribution of solid material units measured at $Q = 3\ \mu L/min$ ($Pl = 0.01$) along (squares) and across (circles) the flow direction. The full lines are exponential fitting functions (see text for discussion). (b) Correlation distances measured along (squares) and across (circles) the flow direction. The error bars indicate the confidence intervals of the exponential fittings according to Eq. 7.

Regardless the flow rate, the distributions of the solid material units in the flow are stronger correlated along the flow direction than along the transversal direction. The slight de-correlation observed in the transversal flow direction may be related to secondary motion of the solid material units located around the centreline of the channel where the velocity gradients are practically vanishing small and rigid gel blobs are allowed to tumble and move across the main flow direction.

4. Conclusions, outlook

A detailed in-situ experimental investigation of the space-time dynamics of solid and fluid elements of a Carbopol gel flowing in a confined plane micro-channel is reported for the first time. A special chemical synthesis protocol that allows one to permanently stain the Carbopol molecules with a fluorescent die (Rhodamine B) was developed in this purpose. This, combined with a state of art image processing tool implemented in the house under Matlab, allows the in-situ detection of solid and fluid material units during the flow. Simultaneously with this, flow fields are measured using a home made $DPIV$ tool by seeding the fluid with a small amount of fluorescent spheres and illuminating with a different wave length for each the Rhodamine stained gel is invisible. The $DPIV$ measurements reveal a plug flow which is a clear signature of a viscoplastic flow behaviour, Figs. 5(b). Due to the spatial confinement of the flow (the depth of the micro-channel is $50\mu m$), solid blobs of the gel locally block the flow and ultimately trigger a secondary flow along the y direction Figs. 4, 5(a). A more systematic investigation of this rather unexpected effect of the flow confinement will be reported elsewhere. Systematic measurements of the statistics of the solid material units in the flow reveal a Weibull distribution characterised by

two parameters, Fig. 6: the scale parameter λ and the shape parameter k. The scale parameter λ does not depend on the flow rate and the shape parameter k decreases slightly with increasing flow rate, Fig. 7. Upon an increase of the mean flow speed (or a decrease of the plasticity number), a partial yielding of the material is observed in terms of a decrease of the space-time average volume fraction of the solid material units $\langle \Phi(\overrightarrow{r}, t) \rangle_{\overrightarrow{r},t}$, Fig. 8(a).

The average size of the solid material units in the flow follows a sigmoidal shaped statistical distribution which is independent on the mean flow rate the plasticity number, Fig. 8(b). This corroborates well with the invariance of the scale parameter of the Weibull distribution with the flow rates and indicates that the increase of wall shear rates associated to the increase of the flow rate do not suffice to further fragment the solid material units of the Carbopol gel. The space-time diagrams describing the microscopic scale dynamics of the solid/fluid material units in the flow presented in Fig. 9 reveal a temporally random behaviour. Conceptually speaking, this confirms the theoretical suggestion advanced in Refs. [36, 37, 8] that the appropriate conceptual framework to understand the microscopic yielding of a viscoplastic material is a statistical one.

A first statistical quantity useful in describing the dynamics of the solid-fluid material is the temporal correlation function. Measurements of the time correlation functions indicate that the dynamics of the solid/fluid material elements are longer correlated in the boundary of the flow than in the bulk, Figs. 10(a), 10(b). This is due to the fact that the lack of shear in the bulk of the flow allows for additional degrees of freedom of the motion of solid material elements such as tumbling and cross-flow motion whereas due to the strong shear near the boundary only the translational degree of freedom (along the mean flow direction) is allowed.

A second statistical quantity our experiments allow one to assess is the spatial correlation function of the solid materials elements. The space correlation surfaces exhibit a clear spatial anisotropy as the flow rate is gradually increased, Fig. 11. The fluctuations of the volume fraction of solid are longer correlated along the flow direction than across the flow direction, Fig. 12(a). Both correlation functions along the flow direction and transversal to the flow direction are independent on the flow rate, (see Supplemental material). The correlation distances along the flow direction Δx_c are systematically larger than the correlation distances across the flow direction Δy_c and they are both insensitive to the flow rate, Fig. 12(b).

The novel measurements of the in-situ spatial and temporal statistics of the distributions of solid/fluid material elements during the confined flow of a Carbopol gel in a plane micro-channel opens several new avenues which, if pursued, could lead to an improved understanding of flows of viscoplastic materials and, in particular, of the solid-fluid transition. As it is clear from this study that microscopic dynamics of solid-fluid interfaces in the flow are best described within a statistical framework rather via deterministic laws typically used to capture the macroscopic flow picture, the results presented herein may be useful in formulating a novel statistical physical picture of the solid-fluid transition that

describes the space time evolution of the volume fraction of the solid Φ during a laminar flow. As already discussed through the paper, a first step in this direction has already been made in Refs. [36, 37, 8] where an analogy between the microscopic yielding and the Ising picture of ferromagnetism was established. This analogy allowed one to assess the statistics of the volume fraction of solid Φ as a function of the external energy input solely based on first principles. A natural generalisation of this picture would be add a flow.

A second interesting avenue to explore relates to understanding the wall slip behaviour of a physical gel during a microscopic flow along smooth walls. It is generally believed that the wall slip during flows of a physical gel along smooth solid surfaces emerges due to the presence of a thin layer of solvent of width δ depleted in the vicinity of the solid walls, [2, 26, 22, 51]). Meeker and coworkers have used such an assumption to rationalise their experimental observations on the wall slip and derive scaling laws by proposing a micro-elasto-hydrodynamic lubrication picture, [22]. The central assumption behind such phenomenological approach is the existence of a depleted layer of solvent of width δ in the vicinity of the solid surface. A similar approach to the wall slip behaviour was undertaken by Seth and coworkers, [40]. As in Ref. [22], macro-rheological observations of the wall slip are rationalised within the framework of an elasto-hydrodynamic lubrication model with the same assumption on the presence of a depleted layer of solvent in the vicinity of the solid surface. For the case of a Carbopol gel, however, we are not aware of any direct visualisation of this layer of solvent. More recently, a systematic experimental investigation of the scaling behaviour of the slip velocity, wall shear stress and wall velocity gradients during a plane micro-channel flow was conducted, [49]. To assess the scaling behaviour in the proximity of the wall, no assumption on the presence of a depleted layer of solvent near the wall was made. Instead, the wall shear stresses were computed by simply connecting in-situ measurements of the wall velocity gradients to a macro-rheological flow curve which allowed one to obtain the wall shear stress. As a result, the scaling laws obtained via this procedure depart significantly from the scaling results previously obtained by others. At this point it is rather clear that the assumption on the presence of a solvent layer near the wall needs to be brought into question. The results presented herein clearly indicate that, in the case of a Carbopol gel, such layer of a constant (in time) width δ can not observed. Indeed, as illustrated in Fig. 3, some of the solid material elements may come in direct contact with the solid walls at some positions downstream whereas other solid elements are separated from the wall by pockets of solvent. Moreover, at a given position downstream, the alternation between solid material elements in contact with the wall and pockets of solvent advected downstream near the wall appears to be random in time, Fig. 9. To picture the dynamics of these events, we refer the reader to the movie added as a supplemental material. These in-situ observations clearly prompt revisiting the theoretical framework of the wall slip behaviour of a physical gel as well.

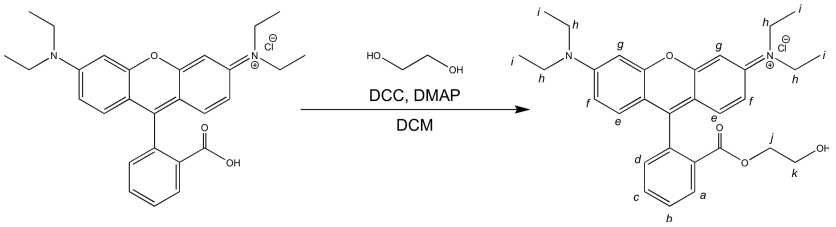

Figure A.13: Preparation of 2-hydroxyethyl ester of Rhodamine B.

5. Acknowledgements

We gratefully acknowledge the Agence Nationale de la Recherche (ANR) for the financial support via project NaiMYS ($ANR-16-CE06-0003$). T.B. gratefully acknowledges a visiting fellowship from the Institute of Macromolecular Chemistry, Czech Academy of Sciencies, Prague which led to the joint development of novel the covalent staining procedure of the Carbopol gel. One of us (T.B.) is deeply indebted to Professor Ian Alistair Frigaard for a number of insightful and motivating discussions on the microscopic yielding of Carbopol gels which have partly motivated the present contribution.

6. Author contributions

The project was designed/initiated/coordinated by T.B. All microfluidic experiments and the rheological measurements were carried on by E.Y. The chemical protocol for the covalent labelling of the Carbopol micro-structure as well as the spectroscopic measurements were jointly designed and implemented by M.H. and Z.S. The data were jointly analysed by E.Y. and T.B. The paper was written by T.B. All authors have participated in reading and improving the initial draft.

Appendix A. Fluorescent labelling of the Carbopol micro-structure

The key point of the experiments reported herein was to permanently stain the Carbopol backbone with a fluorescent compound which allows one to monitor in-situ the spatial distribution of the volume fraction of solid material elements Φ. We describe in detail this novel chemical procedure in the following. Rhodamine B was covalently bound to the Carbopol backbone by a three-step synthesis. In the first step the Rhodamine B was esterified with ethylene glycol providing its 2-hydroxyethyl ester of Rhodamine B, Fig. A.13, as described by Liu et.al, [19].

Ethylene glycol ($0.646\ g$, $10.4\ mmol$), N,N'-dicyclohexylcarbodiimide DCC ($0.516g$, $2.5\ mmol$) and N,N-dimethyl-4-aminopyridine DMAP ($0.031\ g$, $0.25\ mmol$) were dissolved in $20ml$ of dichloromethane (DCM), followed by the drop-wise addition of Rhodamine B ($1\ g$, $2.1\ mmol$) DCM solution ($20\ ml$). The mixture

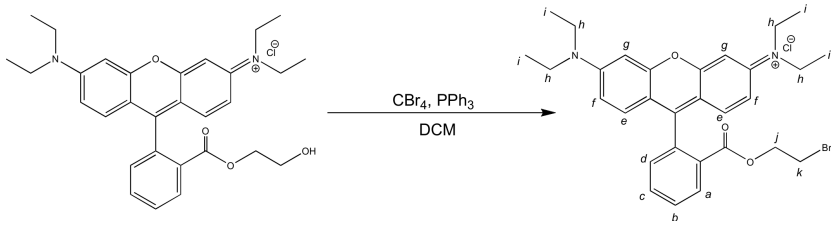

Figure A.14: Preparation of 2-bromoethyl ester of Rhodamine B.

was stirred at room temperature for 12 h. The resulting product was washed by diluted hydrochloric acid for three times to remove excessive ethylene glycol. The organic layer was then dried over anhydrous MgSO4, filtered and evaporated to dryness to give 0.95 g of Rhodamine B ethylene glycol ester (87 % yield) as a purple solid.

The ^1HNMR spectrum of Rhodamine B ethylene glycol ester can be summarised as follows:

$^1H\ NMR(CDCl3, 298\ K, 300\ MHz), \delta(ppm) : 8.40(m, 1H, a)$,
$7.74(m, 2H, bandc), 7.24(m, 1H, d), 7.11(d, 2H, J = 9.37\ Hz, f), 6.87(d, 2H, J = 9.37\ Hz, e), 6.82(s, 2H, g), 4.12(t, 2H, J = 4.40\ Hz, j)$,
$3.45 - 3.70(m, 10H, handk), 1.20 - 1.40(m, 12H, i)$.

The measured ^1HNMR spectrum of Rhodamine B ethylene glycol ester corresponds with the same spectrum reported in literature, [19]. Position of individual protons in the rhodamine B ethylene glycol ester molecule are indicated in italics letters (the last letter in bracket). In the spectrum description, the first number indicates the chemical shift of the signal in ppm. The first letter in brackets stands for the signal multiplicity (typically: s-singlet, d-doublet, t-triplet, m-multiplet, etc.). The multiplicity of the proton signal depends on the number of other non-equivalent hydrogen nuclei in its vicinity. The next value represents the number of interacting nuclei (1H, 2H. . . , etc.) that corresponds to the integral peak area in the spectrum (the integral peak areas are proportional to the number of individual protons in the molecule). For doublets and triplets, the coupling constant in Hz is given. Eleven proton signals can be expected in the ^1HNMR spectrum of Rhodamine B ethylene glycol ester (each chemically non-equivalent proton will appear as a signal). Some signals with similar chemical shifts may overlap with other signals (b and c, h and k).

The 2-hydroxyethyl ester of Rhodamine B obtained in the first step was subsequently transformed to 2-bromoethyl ester, Fig. A.14.

Triphenylphosphine (82 mg, 0.312 $mmol$) and tetrabromomethane CBr4 (104 mg, 0.312 $mmol$) were dissolved in DCM (20 ml), followed by the dropwise addition of Rhodamine B ethylene glycol ester (136 mg, 0.26 $mmol$) DCM solution (20 ml). The reaction mixture was stirred at room temperature for 12 h and then evaporated to dryness. Water (20 ml) was added to crude reaction mixture and precipitated triphenylphosphine oxide was filtered off. After

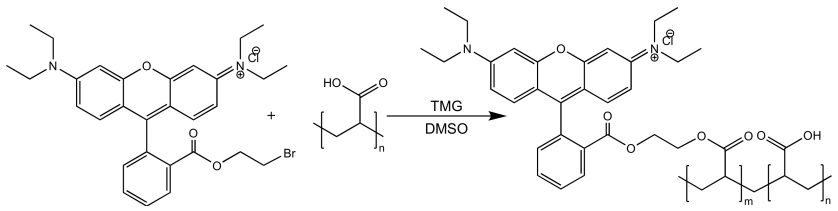

Figure A.15: Grafting of the Rhodamine B 2-bromoethyl ester to Carbopol.

evaporation of filtrate 150 mg (98 % yield) of Rhodamine B 2-bromoethyl ester was obtained as a purple solid.

^1HNMR spectrum of Rhodamine B 2-bromoethyl ester and can be summarised as follows:

$^1H\ NMR(CDCl3, 298\ K, 300\ MHz), \delta(ppm) : 8.40(m, 1H, a)$,
$7.74(m, 2H, bandc), 7.24(m, 1H, d), 7.11(d, 2H, J = 9.37\ Hz, f), 6.87(d, 2H, J =$
$9.37\ Hz, e), 6.82(s, 2H, g), 4.12(t, 2H, J = 4.40\ Hz, j), 3.78(m, 2H, k)$,
$3.50 - 3.70(m, 8H, h), 1.24 - 1.45(m, 12H, i)$.

Due to the high similarity of the molecular structures of Rhodamine B ethylene glycol ester and Rhodamine B 2-bromoethyl ester, very similar ^1HNMR spectra can be expected (most signals will have similar chemical shifts and multiplicity). These structures differ only in the presence of different functional groups ($-CH_2OHand - CH_2Br$) contained in the ester molecule. In the ^1HNMR spectrum of Rhodamine B 2-bromoethyl ester, a change in the chemical shift of protons k can be observed, as expected. This change no longer results in k (3.78 ppm) overlap with proton h (3.50-3.70 ppm) as in the previous case. This indicates the presence of aother functional group (in this case $-CH_2Br$) in the structure.

Finally, the Rhodamine B 2-bromoethyl ester was grafted to the Carbopol backbone following the procedure inspired by Li et al. [18] who descibed the alkylation of polyacrylic acid with low molecular weight alkyl and aryl halides, Fig. A.15.

Rhodamine B bromo derivative (150 mg, 0.256 $mmol$) and subsequently N, N, N', N'-tetramethylguanidine TMG (125 μl, 1 $mmol$) were added to a suspension of Carbopol (3 g) in dimethylsulfoxide DMSO (500 ml). After addition of TMG the reaction mixture became gel-like and was stirred at room temperature overnight. The reaction mixture was then neutralized with 1 N acetic acid. The resulting polymer was precipitated using a large amount of ethyl acetate and collected by filtration. The product was washed three times by ethyl acetate and dried under vacuum at 50 ^oC. In this way 2.7 g of purple solid was obtained.

References

[1] Balmforth, N.J., Frigaard, I.A., Ovarlez, G., 2014. Yielding to stress: Recent developments in viscoplastic fluid mechanics. Annual Review of Fluid Mechanics 46, 121–146. URL: https://doi.org/10.1146/annurev-fluid-010313-141424, doi:10.1146/annurev-fluid-010313-141424, arXiv:https://doi.org/10.1146/annurev-fluid-010313-141424.

[2] Barnes, H.A., 1995. A review of the slip (wall depletion) of polymer solutions, emulsions and particle suspensions in viscometers: its cause, character, and cure. Journal of Non-Newtonian Fluid Mechanics 56, 221 – 251. URL: http://www.sciencedirect.com/science/article/pii/037702579401282M, doi:https://doi.org/10.1016/0377-0257(94)01282-M.

[3] Bingham, E., 1922. Fluidity and Plasticity. McGraw-Hill.

[4] Blackwell, B.C., Ewoldt, R.H., 2014. A simple thixotropic-viscoelastic constitutive model produces unique signatures in large-amplitude oscillatory shear (laos). Journal of Non-Newtonian Fluid Mechanics 208-209, 27 – 41. URL: http://www.sciencedirect.com/science/article/pii/S0377025714000469, doi:http://dx.doi.org/10.1016/j.jnnfm.2014.03.006.

[5] Bonn, D., Denn, M.M., Berthier, L., Divoux, T., Manneville, S., 2017. Yield stress materials in soft condensed matter. Rev. Mod. Phys. 89, 035005. URL: https://link.aps.org/doi/10.1103/RevModPhys.89.035005, doi:10.1103/RevModPhys.89.035005.

[6] Brown, W.K., Wohletz, K.H., 1995. Derivation of the weibull distribution based on physical principles and its connection to the rosin–rammler and lognormal distributions. Journal of Applied Physics 78, 2758–2763. URL: https://doi.org/10.1063/1.360073, doi:10.1063/1.360073, arXiv:https://doi.org/10.1063/1.360073.

[7] Burghelea, T., Bertola, V., 2019. Transport phenomena in complex fluids. Springer International Publishing.

[8] Burghelea, T., Moyers-Gonzalez, M., Sainudiin, R., 2017. A nonlinear dynamical system approach for the yielding behaviour of a viscoplastic material. Soft Matter 13, 2024–2039. URL: http://dx.doi.org/10.1039/C6SM02361D, doi:10.1039/C6SM02361D.

[9] Coussot, P., Nguyen, Q.D., Huynh, H.T., Bonn, D., 2002a. Avalanche behavior in yield stress fluids. Phys. Rev. Lett. 88, 175501. URL: http://link.aps.org/doi/10.1103/PhysRevLett.88.175501, doi:10.1103/PhysRevLett.88.175501.

[10] Coussot, P., Nguyen, Q.D., Huynh, H.T., Bonn, D., 2002b. Viscosity bifurcation in thixotropic, yielding fluids. Journal of Rheology 46, 573–589. URL: http://scitation.aip.org/content/sor/journal/jor2/46/3/10.1122/1.1459447, doi:http://dx.doi.org/10.1122/1.1459447.

[11] Dimitriou, C.J., Ewoldt, R.H., McKinley, G.H., 2013. Describing and prescribing the constitutive response of yield stress fluids using large amplitude oscillatory shear stress (laostress). Journal of Rheology (1978-present) 57, 27–70. URL: http://scitation.aip.org/content/sor/journal/jor2/57/1/10.1122/1.4754023, doi:http://dx.doi.org/10.1122/1.4754023.

[12] Dimitriou, C.J., McKinley, G.H., 2014. A comprehensive constitutive law for waxy crude oil: a thixotropic yield stress fluid. Soft Matter 10, 6619–6644. URL: http://dx.doi.org/10.1039/C4SM00578C, doi:10.1039/C4SM00578C.

[13] Dullaert, K., Mewis, J., 2006a. A structural kinetics model for thixotropy. J. Non-Newtonian Fluid Mech. , 21–30.

[14] Dullaert, K., Mewis, J., 2006b. A structural kinetics model for thixotropy. Journal of Non-Newtonian Fluid Mechanics 139, 21–30.

[15] Geraud, B., Bocquet, L., Barentin, C., 2013. Confined flows of a polymer microgel. The European Physical Journal E 36, 30.

[16] Gutowski, I., Lee, D., de Bruyn, J., Frisken, B., 2012. Scaling and mesostructure of carbopol dispersions. Rheologica Acta , 1–10URL: http://dx.doi.org/10.1007/s00397-011-0614-6. 10.1007/s00397-011-0614-6.

[17] Herschel, W., Bulkley, T., 1926. Measurement of consistency as applied to rubbery benzene solutions. Am. Soc. Test Proc. 26, 621–633.

[18] Li, Q., Bao, Y., Wang, H., Du, F., Li, Q., Jin, B., Bai, R., 2013. A facile and highly efficient strategy for esterification of poly(meth)acrylic acid with halogenated compounds at room temperature promoted by 1,1,3,3-tetramethylguanidine. Polym. Chem. 4, 2891–2897. URL: http://dx.doi.org/10.1039/C3PY00155E, doi:10.1039/C3PY00155E.

[19] Liu, J., Li, A., Tang, J., Wang, R., Kong, N., Davis, T.P., 2012. Thermoresponsive silver/polymer nanohybrids with switchable metal enhanced fluorescence. Chem. Commun. 48, 4680–4682. URL: http://dx.doi.org/10.1039/C2CC18069C, doi:10.1039/C2CC18069C.

[20] Liu, Y., Lorusso, D., Holdsworth, D.W., Poepping, T.L., de Bruyn, J.R., 2018. Effect of confinement on the rheology of a yield-stress fluid. Journal of Non-Newtonian Fluid Mechanics 261, 25 – 32. URL: http://www.sciencedirect.com/science/article/pii/S0377025718300776, doi:https://doi.org/10.1016/j.jnnfm.2018.08.002.

[21] Lopes, R., Rodrigues, R.O., Pinho, D., Garcia, V., Schütte, H., Lima, R., Gassmann, S., 2015. Low cost microfluidic device for partial cell separation: Micromilling approach, in: 2015 IEEE International Conference on Industrial Technology (ICIT), pp. 3347–3350. doi:10.1109/ICIT.2015.7125594.

[22] Meeker, S.P., Bonnecaze, R.T., Cloitre, M., 2004. Slip and flow in soft particle pastes. Phys. Rev. Lett. 92, 198302. URL: https://link.aps.org/doi/10.1103/PhysRevLett.92.198302, doi:10.1103/PhysRevLett.92.198302.

[23] Nguyen, Q.D., Boger, D.V., 1992. Measuring the flow properties of yield stress fluids. Annual Review of Fluid Mechanics 24, 47–88. URL: https://doi.org/10.1146/annurev.fl.24.010192.000403, doi:10.1146/annurev.fl.24.010192.000403, arXiv:https://doi.org/10.1146/annurev.fl.24.010192.000403.

[24] Oppong, F.K., de Bruyn, J.R., 2007. Diffusion of microscopic tracer particles in a yield-stress fluid. J. Non-Newtonian Fluid Mech. 142, 104–111.

[25] Oppong, F.K., Rubatat, L., Frisken, B.J., Bailey, A.E., de Bruyn, J.R., 2006. Microrheology and structure of a yield-stress polymer gel. Phys. Rev. E 73, 041405.

[26] Piau, J., 2007. Carbopol gels: Elastoviscoplastic and slippery glasses made of individual swollen sponges: Meso- and macroscopic properties, constitutive equations and scaling laws. Journal of Non-Newtonian Fluid Mechanics 144, 1 – 29. URL: http://www.sciencedirect.com/science/article/pii/S0377025707000687, doi:10.1016/j.jnnfm.2007.02.011.

[27] Picard, G., Ajdari, A., Bocquet, L., Lequeux, F., 2002. Simple model for heterogeneous flows of yield stress fluids. Phys. Rev. E 66, 051501. URL: http://link.aps.org/doi/10.1103/PhysRevE.66.051501, doi:10.1103/PhysRevE.66.051501.

[28] Poumaere, A., Moyers-Gonzalez, M., Castelain, C., Burghelea, T., 2014. Unsteady laminar flows of a carbopol gel in the presence of wall slip. Journal of Non-Newtonian Fluid Mechanics 205, 28 – 40. URL: http://www.sciencedirect.com/science/article/pii/S0377025714000147, doi:http://dx.doi.org/10.1016/j.jnnfm.2014.01.003.

[29] Putz, A.M.V., Burghelea, T.I., 2009. The solid-fluid transition in a yield stress shear thinning physical gel. Rheol Acta 48, 673–689.

[30] Putz, A.M.V., Burghelea, T.I., Frigaard, I.A., Martinez, D.M., 2008. Settling of an isolated spherical particle in a yield stress shear thinning fluid. Phys. Fluids , 033102.

[31] Quemada, D., 1998a. Rheological modeling of complex fluids: III: Dilatant behaviour of stabilized suspensions. Eur. Phys. J. AP , 309–320.

[32] Quemada, D., 1998b. Rheological modeling of complex fluids: I:The concept of effective volume fraction revisited. Eur. Phys. J. AP , 119–127.

[33] Quemada, D., 1999. Rheological modeling of complex fluids: IV: Thixotropic and "thixoelastic" behaviour. Start-up and stress relaxation, creep tests and hysteresis cycles. Eur. Phys. J. AP , 191–207.

[34] Raffel, M., Willert, C.E., Wereley, S.T., Kompenhans, J., September 2007. Particle Image Velocimetry: A Practical Guide (Experimental Fluid Mechanics). Springer; 2nd edition.

[35] Roussel, N., Le Roy, R., Coussot, P., 2004. Thixotropy modelling at local and macrsocopic scales. J. non-Newtonian Fluid Mech. 117, 85–95.

[36] Sainudiin, R., Moyers-Gonzalez, M., Burghelea, T., 2014. A microscopic gibbs field model for the macroscopic behavior of a viscoplastic fluid. UCDMS Research Report 2014/1 , 1–17URL: http://www.math.canterbury.ac.nz/~r.sainudiin/preprints/20140825_MicroNNF.pdf.

[37] Sainudiin, R., Moyers-Gonzalez, M., Burghelea, T., 2015a. A microscopic gibbs field model for the macroscopic yielding behaviour of a viscoplastic fluid. Soft Matter 11 (27), 5531–5545.

[38] Sainudiin, R., Moyers-Gonzalez, M., Burghelea, T., 2015b. A microscopic gibbs field model for the macroscopic yielding behaviour of a viscoplastic fluid. Soft Matter 11, 5531–5545. URL: http://dx.doi.org/10.1039/C5SM00857C, doi:10.1039/C5SM00857C.

[39] Scarano, F., Rhiethmuller, M.L., 2001. Advances in iterative multigrid piv image processing. Exp. Fluids 29.

[40] Seth, J.R., Cloitre, M., Bonnecaze, R.T., 2008. Influence of short-range forces on wall-slip in microgel pastes. Journal of Rheology 52, 1241–1268. URL: https://doi.org/10.1122/1.2963135, doi:10.1122/1.2963135, arXiv:https://doi.org/10.1122/1.2963135.

[41] de Souza Mendes, P.R., 2009. Modeling the thixotropic behavior of structured fluids. Journal of Non-Newtonian Fluid Mechanics 164, 66 – 75. URL: http://www.sciencedirect.com/science/article/pii/S0377025709001578, doi:http://dx.doi.org/10.1016/j.jnnfm.2009.08.005.

[42] de Souza Mendes, P.R., 2011. Thixotropic elasto-viscoplastic model for structured fluids. Soft Matter 7, 2471–2483. URL: http://dx.doi.org/10.1039/C0SM01021A, doi:10.1039/C0SM01021A.

[43] Tarlet, D., Younes, E., Roux, S., Levy, A., Burghelea, T., 2019. Stopping of a solid object in an elasto viscoplastic material. Journal of Non-Newtonian Fluid Mechanics 263, 120 – 129. URL: http://www.sciencedirect.com/science/article/pii/S0377025718301150, doi:https://doi.org/10.1016/j.jnnfm.2018.11.006.

[44] Thompson, R.L., Soares, E.J., 2016. Viscoplastic dimensionless numbers. Journal of Non-Newtonian Fluid Mechanics 238, 57–64. URL: https://www.sciencedirect.com/science/article/pii/S0377025716300465, doi:https://doi.org/10.1016/j.jnnfm.2016.05.001. viscoplastic Fluids: From Theory to Application 2015 (VPF6).

[45] Thorsen, T., Maerkl, S.J., Quake, S.R., 2002. Microfluidic large-scale integration. Science 298, 580–584. URL: http://science.sciencemag.org/content/298/5593/580, doi:10.1126/science.1076996, arXiv:http://science.sciencemag.org/content/298/5593/580.full.pdf.

[46] Varchanis, S., Makrigiorgos, G., Moschopoulos, P., Dimakopoulos, Y., Tsamopoulos, J., 2019. Modeling the rheology of thixotropic elasto-visco-plastic materials. Journal of Rheology 63, 609–639. URL: https://doi.org/10.1122/1.5049136, doi:10.1122/1.5049136, arXiv:https://doi.org/10.1122/1.5049136.

[47] Weber, E., Moyers-Gonzalez, M., Burghelea, T.I., 2012. Thermorheological properties of a carbopol gel under shear. Journal of Non-Newtonian Fluid Mechanics 183-184, 14 – 24. URL: http://www.sciencedirect.com/science/article/pii/S0377025712001322, doi:10.1016/j.jnnfm.2012.07.005.

[48] Weibull, W., 1939. A Statistical Theory of the Strength of Materials. Generalstabens Litografiska Anstalts Förlag, Stockolm.

[49] Younes, E., Bertola, V., Castelain, C., Burghelea, T., 2020a. Slippery flows of a Carbopol gel in a microchannel. Phys. Rev. Fluids 5, 083303. URL: https://link.aps.org/doi/10.1103/PhysRevFluids.5.083303, doi:10.1103/PhysRevFluids.5.083303.

[50] Younes, E., Himl, M., Stary, Z., Bertola, V., Burghelea, T., 2020b. On the elusive nature of carbopol gels: "model", weakly thixotropic, or time-dependent viscoplastic materials? Journal of Non-Newtonian Fluid Mechanics 281, 104315. URL: http://www.sciencedirect.com/science/article/pii/S0377025720300835, doi:https://doi.org/10.1016/j.jnnfm.2020.104315.

[51] Zhang, X., Lorenceau, E., Basset, P., Bourouina, T., Rouyer, F., Goyon, J., Coussot, P., 2017. Wall slip of soft-jammed systems: A generic simple shear process. Phys. Rev. Lett. 119, 208004. URL: https://link.aps.org/doi/10.1103/PhysRevLett.119.208004, doi:10.1103/PhysRevLett.119.208004.